International Journal of Applied Earth Observation and Geoinformation 122 (2023) 103437

Contents lists available at ScienceDirect

International Journal of Applied Earth Observation and Geoinformation

journal homepage: www.elsevier.com/locate/jag

NIR_vP as a remote sensing proxy for measuring gross primary production across different biomes and climate zones: Performance and limitations

Siyuan Chen [a,b,c], Lichun Sui [b], Liangyun Liu [a,c,*], Xinjie Liu [a,c], Jonathan Li [d], Lingxiao Huang [e,f], Xing Li [g], Xiaojin Qian [h]

[a] International Research Center of Big Data for Sustainable Development Goals, Beijing 100094, China
[b] College of Geological Engineering and Geomatics, Chang' an University, Xi'an 710054, China
[c] Key Laboratory of Digital Earth Science, Aerospace Information Research Institute, Chinese Academy of Sciences, Beijing 100094, China
[d] Department of Geography and Environmental Management, University of Waterloo, Waterloo N2L 3G1, Canada
[e] State Key Laboratory of Resources and Environment Information System, Institute of Geographic Sciences and Natural Resources Research, Chinese Academy of Sciences, Beijing 100101, China
[f] University of Chinese Academy of Sciences, Beijing 100101, China
[g] Research Institute of Agriculture and Life Sciences, Seoul National University, Seoul 08826, Republic of Korea
[h] School of Geographic and Biologic Information, Nanjing University of Posts and Telecommunications, Nanjing 210023, China

ARTICLE INFO

Keywords:
Gross primary production
Light use efficiency
Near-infrared radiation reflected by vegetation
Biomes
Climate zones

ABSTRACT

The product of near-infrared radiation reflected by vegetation (NIR_v) and PAR (NIR_vP) is a promising proxy for the remote estimation of gross primary production (GPP). However, the efficiency of NIR_vP in estimating the GPP and its limitations across multiple biomes and climate zones remain unclear. In this study, we aimed to evaluate the performance and limitations of NIR_vP in estimating the GPP in comparison to absorbed photosynthetically active radiation (APAR), solar-induced chlorophyll fluorescence (SIF), and the MOD17A2H GPP product. Overall, the correlation between NIR_vP and eddy covariance (EC) GPP was stronger than that of APAR, SIF, and MOD17A2H GPP across most biomes with usually similar seasonal variations in radiation, air temperature (TA), and precipitation. The near-infrared (NIR) reflectance (ρ_{NIR}) and light use efficiency (LUE) exhibited a covarying relationship under these environmental conditions, which suggested that the ρ_{NIR} contributed positively to the NIR_vP-GPP relationship under such climatic conditions. However, the performance of NIR_vP was poor in some biomes and climate zones, which exhibited different variations in the seasonal patterns of radiation, TA, and precipitation. The resulting inconsistencies between ρ_{NIR} and LUE implied that the ρ_{NIR} contributed negatively to the NIR_vP-GPP relationship in these regions. Altogether, the findings demonstrated that the NIR_vP-GPP relationship was robust but attained a moderate overall relationship across ecosystems ($R^2 < 0.50$) in the majority of biomes and climate zones. In addition, this study also elucidated the limitations of NIR_vP as a GPP proxy in certain climate zones, which was attributed to the synergistic contributions of APAR and ρ_{NIR} in the NIR_vP-GPP relationship.

1. Introduction

The gross primary production (GPP) plays a key role in the functioning of terrestrial ecosystems and serves as an important indicator for monitoring the global carbon cycle (Ballantyne et al., 2012; Lin et al., 2022; Lin et al., 2021). Various methods developed for the quantification of terrestrial GPP using remote sensing data have been applied over regional and global scales (Xiao et al., 2019). Of these methods, the light use efficiency (LUE)-based models are extensively used for estimating the GPP (Coops et al., 2010; Medlyn, 1998; Monteith, 1972, 1977; Yang et al., 2022). LUE-based models use the product of the incoming photosynthetically active radiation (PAR), the fraction of PAR absorbed by the vegetation (FAPAR), the maximum LUE, and major environmental stress factors, including temperature and various parameters related to water and carbon dioxide, for calculating the GPP (Xiao et al., 2019). However, LUE-based models have considerable uncertainties

* Corresponding author at: Aerospace Information Research Institute, Chinese Academy of Sciences, No. 9 Dengzhuang South Road, Haidian District, Beijing 100094, China

E-mail address: liuly@radi.ac.cn (L. Liu).

https://doi.org/10.1016/j.jag.2023.103437
Received 5 April 2023; Received in revised form 20 June 2023; Accepted 24 July 2023
Available online 28 July 2023

owing to the model inputs of FAPAR (Liu et al., 2019; Running et al., 2000; Tao et al., 2015) and LUE (Running et al., 1999; Ryu et al., 2019; Yuan et al., 2014).

The recently developed solar-induced chlorophyll fluorescence (SIF) method provides alternative approaches for estimating GPP over global scales (Badgley et al., 2017; Guanter et al., 2014) by providing physiological and biochemical information (Porcar-Castell et al., 2014) regarding the vegetation under study. Satellite-based SIF datasets have therefore been extensively used as an indicator for measuring global GPP (Guanter et al., 2014; Mohammed et al., 2019; Ryu et al., 2019). However, the relationship between SIF and GPP may vary due to different canopy structures (van der Tol et al., 2019; Yang et al., 2019) and sun-sensor geometry effects (Zhang et al., 2021), and relies strongly on the fluorescence emission efficiency and LUE. Furthermore, the SIF-based estimation of GPP is also limited by the weak signal-to-noise ratio (SNR) and coarse spatial resolution of the currently available SIF products (Frankenberg et al., 2011; Joiner et al., 2013; Sun et al., 2017; Köhler et al., 2020; Li et al., 2019).

Owing to its superior ability and unique characteristics in vegetation canopy structure, the near-infrared (NIR) reflectance (ρ_{NIR}) of vegetation (NIR_v) (Huete, 1988; Major et al., 1990; Badgley et al., 2017; Zeng et al., 2019) has gathered much attention. The ρ_{NIR} has been incorporated in numerous applications owing to its clear physical foundation and strong correlation with vegetation photosynthesis (such as $NIR_v = NDVI \times \rho_{NIR}$) (Badgley et al., 2017; Badgley et al., 2019). Subsequently, the near-infrared radiance of vegetation ($NIR_vR = NDVI \times Rad_{NIR}$) and NIR_vP ($NIR_v \times PAR$) were proposed to further incorporate the radiation factor and obtain a better relationship with both SIF and GPP (Dechant et al., 2020; Dechant et al., 2022). For instance, ρ_{NIR} and NIR radiance-related proxies have been applied for estimating the GPP across multiple spatial and temporal scales and are regarded as robust proxies in estimating GPP (Abdi et al., 2019; Badgley et al., 2019; Badgley et al., 2017; Baldocchi et al., 2020; Dechant et al., 2020; Dechant et al., 2022; Jiang et al., 2021; Liu et al., 2020; Wang et al., 2021).

Mechanistically, NIR-based GPP estimation can be explained from two major viewpoints. First, owing to the strong SIF-GPP relationship from ecosystems to global scales (Xiao et al., 2019), the inclusion of structural and radiation information in NIR_vP as SIF contained (Dechant et al., 2020; Dechant et al., 2022) may explain the superior NIR_vP-GPP relationships. Moreover, NIR_vP is simply estimated as the product of APAR and the fraction of all SIF photons escaping from the canopy, namely APAR $\times f_{esc}$ (Dechant et al., 2022), which provides a superior explanation based on the SIF-GPP relationship and NIR_vP has been found to outperform SIF at rice and corn plantation sites (Zeng et al., 2019; Dechant et al., 2020). However, the reliability of SIF in GPP estimation does not hold true in all cases (Xiao et al., 2019). For instance, SIF has a poor sensitivity in tracking short-term variabilities in photosynthetic efficiency under stressful conditions (Middleton et al., 2016). Wohlfahrt et al. (2018) demonstrated that the alterations in GPP estimated based on the SIF are $<35\%$, and the method has a limited potential in estimating the GPP during heat waves occurring within ten days. Moreover, NIR_vP only includes the canopy structure and radiation factor, and could be more unreliable than SIF for GPP estimation owing to the absence of physiological information. Second, the fact that ρ_{NIR} enables the tracking the of diurnal and seasonal variations in LUE (Liu et al., 2020; Kim et al., 2021) could serve as a basis for using the NIR_vP in GPP estimations. For instance, studies by Liu et al. (2020) and Dechant et al. (2020) indicated that the ρ_{NIR} and LUE exhibit covarying relationships at cropland sites. It has been additionally demonstrated that the NIR-sensitive vegetation index is capable of partially capturing the variabilities in LUE (Wang et al., 2020). However, recent studies have demonstrated that the ρ_{NIR} is ineffective in tracking the GPP of evergreen forests (Cheng et al., 2020; Kim et al., 2021). Nevertheless, the ability of ρ_{NIR} in characterizing the LUE across different biomes and climate zones remains empirically unclear.

These findings imply that although NIR_vP has a superior performance in estimating the GPP owing to the dominant role of APAR, the contribution of ρ_{NIR} to the NIR_vP-GPP relationship remains to be fully elucidated. It is therefore extremely necessary to comprehensively evaluate the performance of NIR_vP and investigate the contribution of ρ_{NIR} to the NIR_vP-GPP relationship for determining the limitations of NIR_vP in estimating the GPP across different biomes and climate zones.

The present study aimed to utilize multi-source remote sensing data for evaluating the performance of NIR_vP in estimating the GPP across different biomes and climate zones over flux sites, and to explore the limitations of NIR_vP based on the additional contribution of ρ_{NIR} to the NIR_vP-GPP relationship except for the dominant role of APAR based on theoretical derivations and experimental data.

2. Materials and methods

2.1. EC data

The publicly available FLUXNET 2015 dataset (Agarwal et al., 2010; Baldocchi et al., 2001) contains several ecosystem fluxes determined using the EC method. A total of 147 FLUXNET sites providing data regarding the different flux variables of GPP (GPP_NT_VUT_REF), incoming shortwave radiation (SW_IN), and climate variables, including air temperature (TA_F) and precipitation (P_F), during a period from 2008 to 2014 that overlapped with the period of the synchronous satellite-based data, were selected. Specifically, data from 18 cropland (CRO), 17 deciduous broadleaf forest (DBF), 11 evergreen broadleaf forest (EBF), 19 evergreen needleleaf forest (ENF), 34 grassland (GRA), nine mixed forest (MF), five open shrubland (OSH), nine savanna (SAV), 19 wetland (WET), and six woody savanna (WSA) sites were retrieved. Fig. S1 depicted the spatial distribution of the selected EC flux sites, and the detailed information, including the site ID, name, latitude, longitude, biomes, and climate types are listed in Table S1.

2.2. Satellite data

2.2.1. FAPAR product

The photosynthetically active radiation (PAR) absorption fraction data was retrieved from the MODIS MCD15A2H V006 product. MCD15A2H is a composite product with a time resolution of 8 days and a spatial resolution of 500 m, and includes the FAPAR, leaf area index (LAI), and quality control (QC) files (Myneni et al., 2005). The main algorithm is based on a 3D radiation transmission model (Knyazikhin et al., 1998), which uses the atmospherically corrected bidirectional reflectance function (BRF) (Vermote et al., 1999) and the look-up table (LUT) method, and the backward algorithm is an empirical model. The final retrieval results represent average values that meet the uncertainty requirements across different biomes and climatic conditions (Myneni et al., 2002).

2.2.2. Downscaled solar-induced chlorophyll fluorescence (DSIF) product

The DSIF product (wavelength: 740 nm) is a continuous SIF dataset (Ma et al., 2022) with a spatial resolution of 0.05°, and is generated from GOME-2 retrievals (Joiner et al., 2013; Joiner et al., 2016). The dataset had a fine spatial resolution (0.05°) and a 16-day temporal resolution, covering the temporal range between February 2007 and March 2019. The DSIF product uses a random forest model, and the training samples are obtained from GOME-2 SIF retrievals combined with related explanatory parameters. The machine learning (ML)-predicted SIF with a spatial resolution of 0.05°, determined using the random forest model, served as a weighting factor for redistributing the original GOME-2 SIF with a spatial distribution of 0.5° and for generating the DSIF dataset with a spatial distribution of 0.05°. The DSIF data was validated for increasing the consistency with the original 0.5° GOME-2 SIF data compared to the ML-predicted SIF dataset derived from GOME-2.

2.2.3. Surface reflectance data

The MCD43A4 Nadir BRDF-Adjusted Reflectance (NBAR) product (Schaaf et al., 2015) was computed for each of the spectral bands of MODIS (1–7) at local solar noon on the day of interest for obtaining the daily NBAR dataset with a resolution of 500 m. In this study, NBAR data at local solar noon was retrieved for MODIS bands 1 and 2 (red, 629–670 nm; and NIR, 841–876) from the Fixed Sites Subsets Tool (DAAC, 2018) (https://modis.ornl.gov/globalsubset/) and used for calculating the NDVI, NIR_vP, and related proxies.

2.2.4. Satellite GPP product

The MOD17A2H version 6 Gross Primary Productivity (GPP) product (Running et al., 2005) is a cumulative 8-day composite dataset with a pixel size of 500 m, and is based on the concept of radiation use efficiency. The algorithm first generates the daily APAR and subsequently determines the biome-specific parameters from the Biome Properties LUT (BPLUT) for each pixel. The maximum LUE values are then attenuated using two environmental scalars. The GPP estimates are finally obtained based on the product of APAR and the attenuated LUE. The MOD17A2H GPP data that corresponded to the selected FLUXNET sites were selected in this study.

2.3. ERA-5 SSRD data

The downward surface solar radiation data are derived from the reanalysis data of the European Centre for Medium-Range Weather Forecasts (ECMWF). ERA-5 is the fifth-generation ECMWF global climate data. Global reanalysis data based on the third-generation climate data of ERA-Interim from 1979 to the present day are currently available (https://www.ecmwf.int/en/forecasts/datasets/reanalysis-datasets/era5). Reanalysis data use the laws of physics and data assimilation methods (4D-Var in case of ERA-5) to combine the observations into a globally complete field. In this study, we selected the surface solar downward radiation (SSRD) data with a spatial resolution of 0.25° and a time resolution of one hour for estimating the PAR with a coefficient of 0.48, which represented the ratio of PAR absorbed by the vegetation to the total solar radiation (McCree, 1972).

2.4. Köppen-Geiger climate classification data

The world map of the Köppen-Geiger climate data is the most frequently used climate classification map, and was first prepared by Geiger (Geiger, 1961). An updated world map of the Köppen-Geiger climate classification data was released (Kottek et al., 2006) and retrieved for analysis in this study. The abbreviations for each biome and climate zone combinations matching the selected FLUXNET sites in our study are provided in Table 1, and the complete climate types in the Köppen-Geiger climate classification scheme are provided in Table S2.

Table 1
Combination and abbreviations of biomes and climate types involved in this study.

Climate types	Biomes	Abbreviations
Equatorial monsoon (Am)	Evergreen broadleaf forest (EBF)	AmEBF
	Deciduous broadleaf forest (DBF)	AmDBF
	Grassland (GRA)	AmGRA
Equatorial savannah with dry winter (Aw)	Grassland (GRA)	AwGRA
	Savanna (SAV)	AwSAV
	Wetland (WET)	AwWET
	Woody savanna (WSA)	AwWSA
Steppe climate (Bs)	Cropland (CRO)	BsCRO
	Deciduous broadleaf forest (DBF)	BsDBF
	Grassland (GRA)	BsGRA
	Mixed forest (MF)	BsMF
	Open shrubland (OSH)	BsOSH
	Savanna (SAV)	BsSAV
	Woody savanna (WSA)	BsWSA
Desert climate (Bw)	Grassland (GRA)	BwGRA
	Open shrubland (OSH)	BwOSH
	Savanna (SAV)	BwSAV
Tundra climate (ET)	Evergreen needleleaf forest (ENF)	ETENF
	Grassland (GRA)	ETGRA
	Open shrubland (OSH)	ETOSH
	Wetland (WET)	ETWET
Snow climate with dry summer (Ds)	Evergreen needleleaf forest (ENF)	DsENF
Warm temperate climate, fully humid (Cf)	Cropland (CRO)	CfCRO
	Deciduous broadleaf forest (DBF)	CfDBF
	Evergreen broadleaf forest (EBF)	CfEBF
	Evergreen needleleaf forest (ENF)	CfENF
	Grassland (GRA)	CfGRA
	Mixed forest (MF)	CfMF
Warm temperate climate with dry summer (Cs)	Cropland (CRO)	CsCRO
	Deciduous broadleaf forest (DBF)	CsDBF
	Evergreen broadleaf forest (EBF)	CsEBF
	Evergreen needleleaf forest (ENF)	CsENF
	Grassland (GRA)	CsGRA
	Wetland (WET)	CsWET
	Woody savanna (WSA)	CsWSA
Snow climate, fully humid (Df)	Cropland (CRO)	DfCRO
	Deciduous broadleaf forest (DBF)	DfDBF
	Evergreen needleleaf forest (ENF)	DfENF
	Grassland (GRA)	DfGRA
	Mixed forest (MF)	DfMF
	Wetland (WET)	DfWET
Snow climate with dry winter (Dw)	Grassland (GRA)	DwGRA
	Wetland (WET)	DwWET

2.5. GPP proxies

2.5.1. SIF

As SIF is a widely proven proxy for GPP (Guanter et al., 2014; Gu et al., 2019), we selected it as a GPP proxy in this study for comparisons with NIR_vP. The SIF observed above canopies is defined as the product of APAR, physiological SIF emission yield of the whole canopy (SIF_{yield}), and the f_{esc}, as depicted in Eq. (1) (Guanter et al., 2014; Zeng et al., 2019). According to the basic definition of SIF, the SIF-GPP relationship is dominated by APAR and the apparent SIF emission yield ($ASIF_{yield} = SIF_{yield} \times f_{esc}$) which combines both vegetation structure and physiological information in characterizing the LUE. We therefore assumed that the $ASIF_{yield}$, which contains additional physiological information compared to ρ_{NIR}, is correlated to the LUE. Furthermore, based on the estimation of f_{esc} as a ratio of NIR_v and FAPAR in Eq. (2) (Zeng et al., 2019), SIF can also be estimated using Eq. (3). Therefore, NIR_vP can also be regarded as a structural and radiation factor as SIF contained (Dechant et al., 2020). In this study, the $ASIF_{yield}$ was determined using Eq. (4), which is derived from Eq. (1), where FAPAR is derived from the MCD15A2H product, and PAR is estimated from the ERA-5 SSRD data using a coefficient of 0.48 (McCree, 1972). However, the value of $ASIF_{yield}$ obtained using this formula does not represent the absolute value, but provides a linear approximation of $ASIF_{yield}$.

$$SIF = APAR \times SIF_{yield} \times f_{esc} = APAR \times ASIF_{yield} \tag{1}$$

$$f_{esc} \approx \frac{NIR_v}{FAPAR} \tag{2}$$

$$SIF \approx APAR \times SIF_{yield} \times \frac{NIR_v}{FAPAR} = NIR_vP \times SIF_{yield} \tag{3}$$

$$ASIF_{yield} = \frac{SIF}{APAR} = \frac{SIF}{FAPAR \times PAR} \quad (4)$$

2.5.2. NIR_vP

The NIR_vP is calculated using the ρ_{NIR} of vegetation (NIR_v) and PAR (Dechant et al., 2022). A theoretical derivation from Eq. (5) revealed that the NIR_vP-GPP relationship is driven by the ratio of NDVI and FAPAR and ρ_{NIR} except for the APAR term, which both characterizing the LUE.

$$NIR_vP = NIR_v \times PAR = NDVI \times \rho_{NIR} \times PAR = APAR \times \frac{NDVI}{FAPAR} \times \rho_{NIR} \quad (5)$$

where NIR_v represents the NIR reflectance of the vegetation, estimated as the product of NDVI and ρ_{NIR} (Badgley et al., 2017); ρ_{NIR} denotes the NIR reflectance extracted from the MODIS reflectance product; and PAR is the photosynthetically active radiation derived from the SSRD data obtained from the ERA-5 dataset using a coefficient of 0.48 (McCree, 1972).

Based on Eq. (5), we can further explore the contribution of ρ_{NIR} to the NIR_vP-GPP relationship except for the dominant role of APAR. The NDVI-FAPAR relationship was found to be linear and robust under different conditions (Myneni and Williams, 1994), which was also demonstrated based on the simulated dataset using SCOPE model (Fig. S2). We therefore assumed that the ratio of NDVI and FAPAR was relatively stable, and the additional information except for APAR in NIR_vP is primarily contributed by the ρ_{NIR} term. Specifically, the ρ_{NIR} may positively contribute to the NIR_vP-GPP relationship when the variations in ρ_{NIR} are consistent with the alterations in LUE, yielding a positive correlation existed between ρ_{NIR} and LUE. On the contrary, the ρ_{NIR} may also reduce the performance of NIR_vP in estimating the GPP when the variations in ρ_{NIR} are inconsistent with the alterations in LUE, resulting a negative correlation or lack of correlation between ρ_{NIR} and LUE. Based on such understandings, we hypothesized that the information in ρ_{NIR} may affect the performance of NIR_vP in estimating the GPP. In this study, the LUE was calculated by combining the satellite data, reanalysis data, and the *in situ* observations retrieved from the FLUXNET dataset, as follows:

$$LUE = \frac{GPP}{APAR} = \frac{GPP}{FAPAR \times PAR} \quad (6)$$

where GPP represents the 16-day average collected from the half-hourly or hourly observations of GPP at each FLUXNET site; FAPAR is derived from the MCD15A2H product using the Fixed Sites Subsets Tool (DAAC, 2018).

2.5.3. APAR

Owing to its strong correlation with vegetation photosynthesis and its dominant role in GPP, APAR was selected as an indicator of GPP in this study. APAR is generally calculated as the product of FAPAR and PAR. In this study, the MODIS FAPAR (MCD15A2H) and ERA-5 SSRD data were used for estimating the APAR as depicted in Eq. (7):

$$APAR = FAPAR \times PAR \quad (7)$$

where FAPAR is derived from MCD15A2H, and PAR is transformed from the SSRD data obtained from ERA-5.

All the proxies and data used for comparing with EC GPP were resampled to the same spatial resolution (0.05°) and temporal resolution (16-day). Prior to evaluating the performance of the different proxies with EC GPP, a correction was performed for resolving the spatial mismatches between the satellite data and the average footprint of the EC data. Specifically, the ratio of 250 m NDVI and 0.05° NDVI was used as the correction ratio (Eq. (8)), based on the assumption that they contained the corresponding EC and satellite scale data.

$$correction\_ratio = \frac{NDVI_{250m}}{NDVI_{0.05^\circ}} \quad (8)$$

$$GPP\_proxy_{corr} = GPP\_proxy \times correction\_ratio \quad (9)$$

2.5.4. Evaluation approach

In this study, linear regression for each single GPP proxy as well as the MODIS GPP with EC GPP was firstly conducted for performance evaluation. Meanwhile, we further conducted multi-variable analysis based on Generalized Linear Model (GLM) (Goetz et al., 2015) in order to explore the importance of each GPP proxy. Statistic metrics including the coefficient of determination (R^2), linear regression slope, standardized regression coefficient and P value (Wilks, 2011) are selected for evaluation (Eyoh et al., 2012; Mitchell et al., 2012; Garzón et al., 2021). The standardized regression coefficient is calculated from the original GLM regression coefficients using the ratio of the standard deviations of GPP proxies and EC GPP (Eq. (10)).

$$b_{j\_Std} = b_j \times \frac{S_j}{S_Y} \quad (10)$$

where b_{j_std} is the standardized regression coefficient, b_j is the original GLM regression coefficient, S_j and S_Y are the standard deviation of each GPP proxy and EC GPP.

Subsequently, we analyzed the correlation of ρ_{NIR} and $ASIF_{yield}$ with LUE across different biomes and climate zones to investigate the effect of ρ_{NIR} in driving the NIR_vP-GPP relationship, except for the dominant role of APAR. The correlation coefficient (R) was determined for quantifying the direction and magnitude of the relationships of ρ_{NIR} and $ASIF_{yield}$ with LUE.

2.6. Linkage and differences among APAR, SIF, and NIR_vP

In this study, three GPP proxies, including NIR_vP, APAR, SIF, and the MOD17A2H satellite GPP product, were selected for comprehensive evaluation of the performance of NIR_vP for GPP estimations. The basic equation for calculating the GPP was proposed by Monteith (Monteith, 1972), where the GPP is defined as the product of PAR absorbed by the canopy (APAR) and the photosynthetic LUE (Eq. (11)). From the theoretical framework it is evident that the variations in GPP are attributed to both APAR and LUE.

$$GPP = FAPAR \times PAR \times LUE = APAR \times LUE \quad (11)$$

An overall analysis of the different GPP proxies (Fig. 1) revealed that they share the same information about APAR, which plays a dominant role in vegetation photosynthesis and can be used for estimating the GPP (Gitelson et al., 2016; Zhang et al., 2020). Specifically, the mechanistic differences among the different proxies for GPP estimation lies in the characterization of LUE, which is based on the unique components of structural information (ρ_{NIR}) in NIR_vP, and both physiological and structural information including SIF_{yield} and f_{esc} in SIF.

3. Results

3.1. Evaluation of the performance of different GPP proxies

3.1.1. Relationships between EC GPP and different GPP proxies

The linear regression results of EC GPP versus the three GPP proxies and the MOD17A2H product across all selected biomes are depicted in Fig. 2. These findings indicated a better performance of NIR_vP than APAR, SIF, and the MOD17 GPP product, with a slightly higher R^2 value of 0.491.

The GLM multi-variable analysis metrics of different combinations of three GPP proxies are shown in Fig. 3. In order to display the p values over a unified magnitude, a logarithmic scale (-log10) is used for better visualization (higher bars indicate lower p values). NIR_vP performed

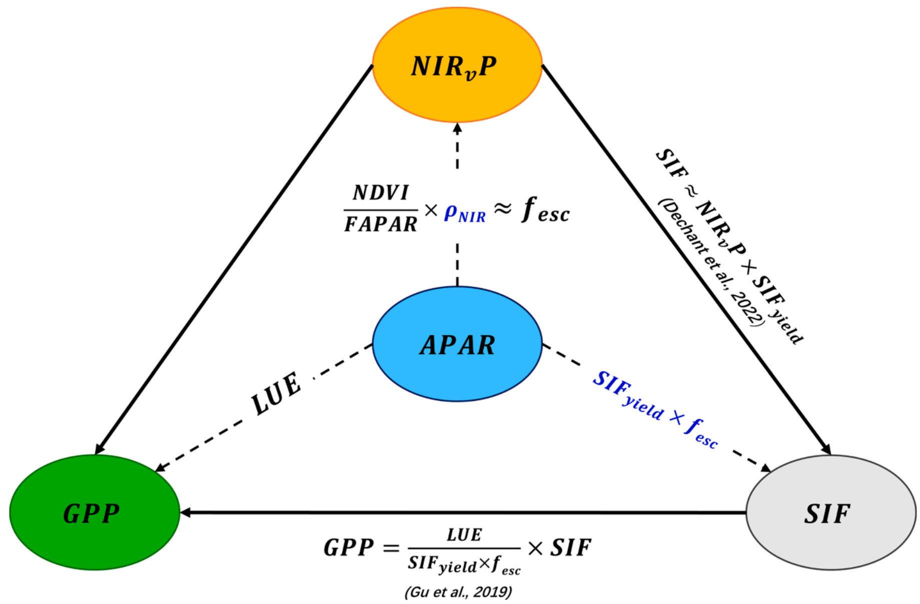

Fig. 1. Overview depicting the conceptual meaning of the different GPP proxies (NIR_vP, SIF, and APAR), and GPP. The letters in blue denote the inclusion of additional information in NIR_vP and SIF, with the exception of the APAR term. (For interpretation of the references to color in this figure legend, the reader is referred to the web version of this article.)

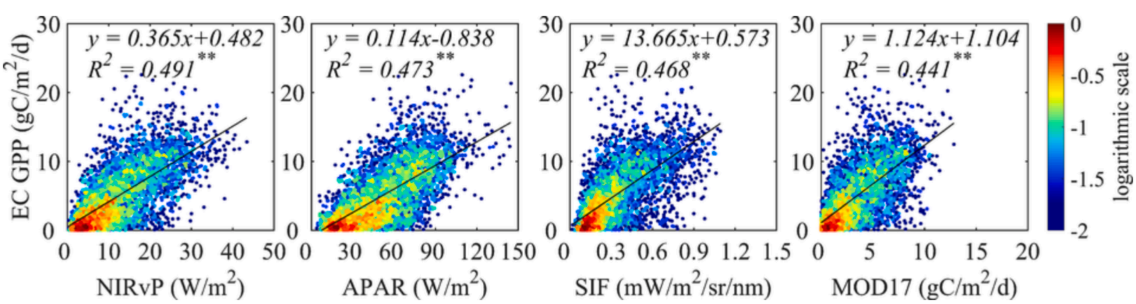

Fig. 2. Relationships of NIR_vP, APAR, SIF, and MOD17A2H GPP with EC GPP across all the selected biomes in the FLUXNET sites. The color bar denotes the relative density of the scatter in a logarithmic scale. $^{**}p < 0.001$.

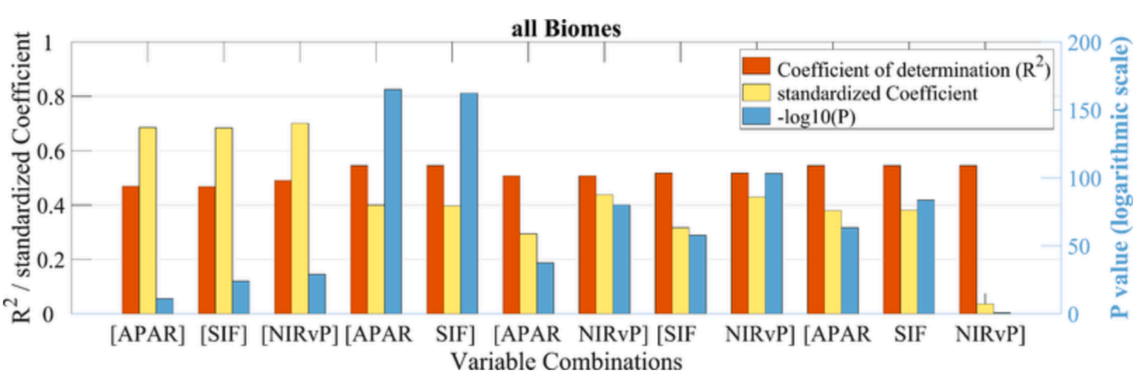

Fig. 3. GLM regression metrics of different combinations of three GPP proxies across all selected biomes in 147 FLUXNET sites. Left axis denotes the R^2 and standardized coefficient, right axis denotes the p values in a logarithmic scale.

best in the single-variable combinations across all selected biomes with the highest R^2, highest standardized coefficient and the smallest p value. Based on the two-variable results, similar R^2 values are noticed within different variable combinations but higher standardized coefficient and smaller p values of NIR_vP can be noticed. It is worth noting that APAR performs almost identically to SIF, with close standardized coefficients and p values in the combination of APAR and SIF. When putting three GPP proxies together, SIF gives best performance with highest standardized coefficient and smallest p values compared to APAR and NIR_vP.

3.1.2. Relationships between EC GPP and different GPP proxies across biomes

Fig. 4 shows the linear regression results of NIR_vP, APAR, SIF, and MOD17 GPP with EC GPP across ten different biomes. The performance

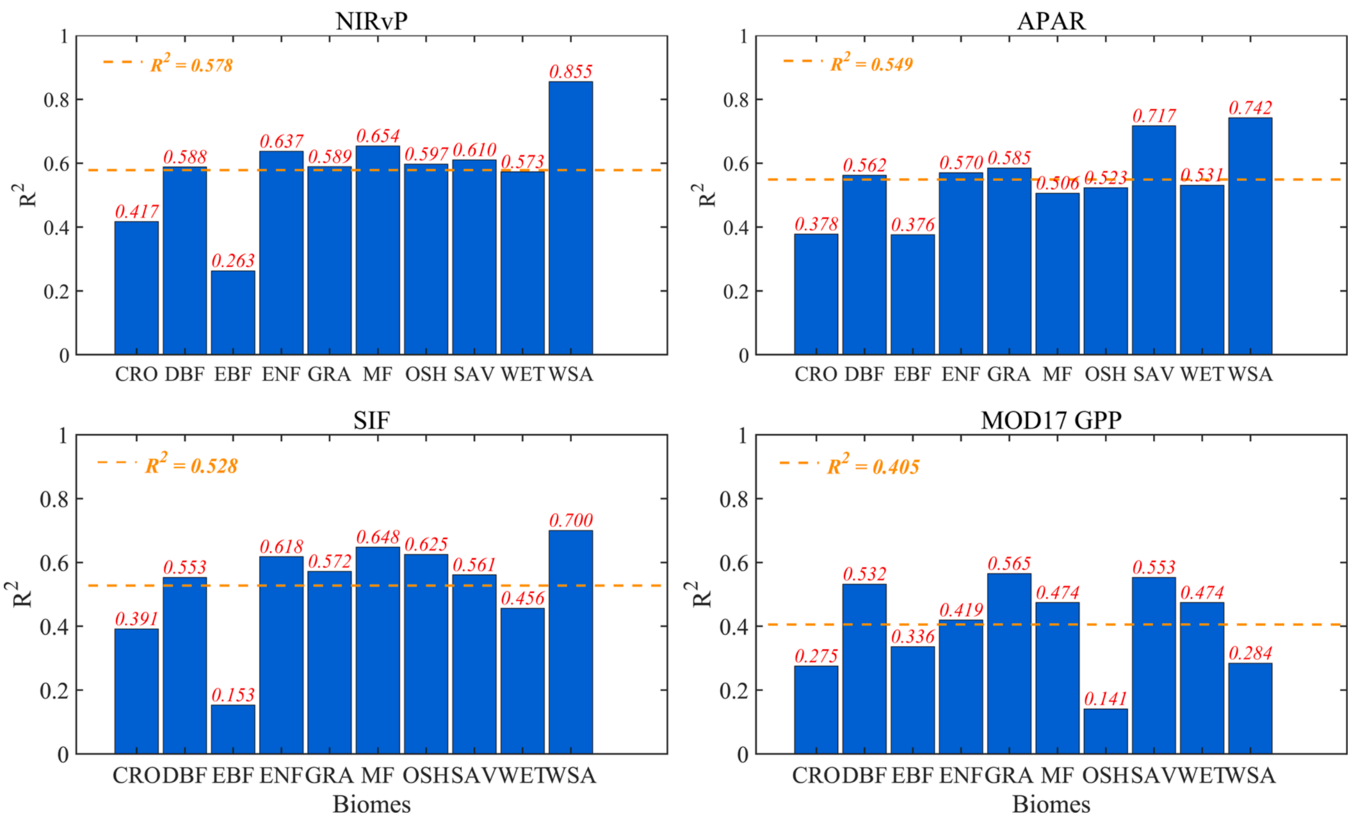

Fig. 4. R^2 values of the GPP proxies and MODIS GPP plotted against EC GPP, across different biomes in the FLUXNET sites (Horizontal dotted lines per panel denote the average R^2 value across all biomes).

of NIR_vP vs. GPP was better across the majority of different biomes, including CRO, DBF, ENF, GRA, MF, and WET, with R^2 values ranging from 0.417 to 0.853. APAR had the strongest relationship with EC GPP in the EBF and SAV biomes, with R^2 values of 0.376 and 0.717, respectively. For OSH, the SIF was the best predictor of EC GPP with an R^2 value of 0.625.

Multi-variable regression results including different combinations of three GPP proxies across ten biomes are displayed in the supplementary material (Fig. S3 and Table S3). Overall, NIR_vP behaved better relationships with EC GPP based on the single-variable and two-variable combinations, with higher R^2, higher standardized coefficients and lower P values over most biomes, except for the GRA, MF, OSH and SAV biome. However, based on the results of three-variable combinations, NIR_vP may not always be the most important variable in characterizing GPP. For example, SIF became the most important variable comparing to APAR and NIR_vP in the DBF, ENF, GRA and MF biome. Besides, APAR was the most significant variable in the EBF and SAV biome.

3.1.3. Relationship between EC GPP and different GPP proxies across climate zones

Linear regression results of different GPP proxies and the MOD17 GPP across different climate zones are shown in Fig. 5. Overall, NIR_vP owned higher R^2 values in 11 of the 31 selected biomes and climate zones compared to other three variables. SIF performed best at eight sites, and APAR is more robust at seven sites with higher R^2 values. In addition, MOD17 GPP explained most of the variation in EC GPP at only three sites.

Multi-variable regression results of three GPP proxies across different biomes and climate zones are listed in Table S4. Overall, the results exhibited a better performance of NIR_vP to GPP in more than half (17) of the selected 31 climate zones. However, APAR and SIF contributed more significantly with higher R^2, higher standardized coefficients and lower P values than NIR_vP respectively in ten and four climate zones.

3.1.4. Variations in the slope of different GPP proxies across biomes

The performance of the different GPP proxies was further compared at the biome scale using linear regression slopes obtained from the EC GPP vs. proxies, and used to calculate the coefficient of variation (CV) across the different biomes (Fig. 6). The overall results demonstrated that the SIF had the smallest CV for the fitted linear regression slopes across the different biomes (0.147), followed by the NIR_vP (0.163), APAR (0.232), and MOD17A2H (0.314).

3.2. Relationships of ρ_{NIR} and $ASIF_{yield}$ with LUE

3.2.1. Correlation of ρ_{NIR} and $ASIF_{yield}$ with LUE across biomes

As depicted in Fig. 7, analysis of the ρ_{NIR}-LUE relationship (blue scatter points) in all the selected biomes except for EBF revealed that the ρ_{NIR} was significantly and positively associated with the corresponding LUE values ($p < 0.05$ and $p < 0.001$), and the correlation coefficients varied from 0.128 to 0.748, but only one biome was higher than 0.5 (WSA). Analysis of the $ASIF_{yield}$-LUE relationship (red scatter points) revealed that $ASIF_{yield}$ was found to be significantly and positively associated with LUE in all biomes, with correlations ranging from 0.119 to 0.567, expect for EBF and WET. The EBF site was negatively correlated for both ρ_{NIR} (−0.396) and $ASIF_{yield}$ (−0.270).

3.2.2. Correlation of ρ_{NIR} and $ASIF_{yield}$ with the LUE across different climate zones

In order to further explore how the ρ_{NIR} and $ASIF_{yield}$ are each related to the LUE, the climate zone data were integrated into the comparative analysis (Fig. 8). In general, ρ_{NIR} and LUE were found to be positively correlated in DBF, OSH, WET, and WSA across the different climate zones. However, negative correlations between ρ_{NIR} and LUE were also noticed in many more sites: {the CsCRO, CfEBF, CsEBF, CfENF, BsGRA, BsMF, BsSAV, and AwSAV} after incorporating the climatic data. Besides, positive correlations between $ASIF_{yield}$ and LUE were only

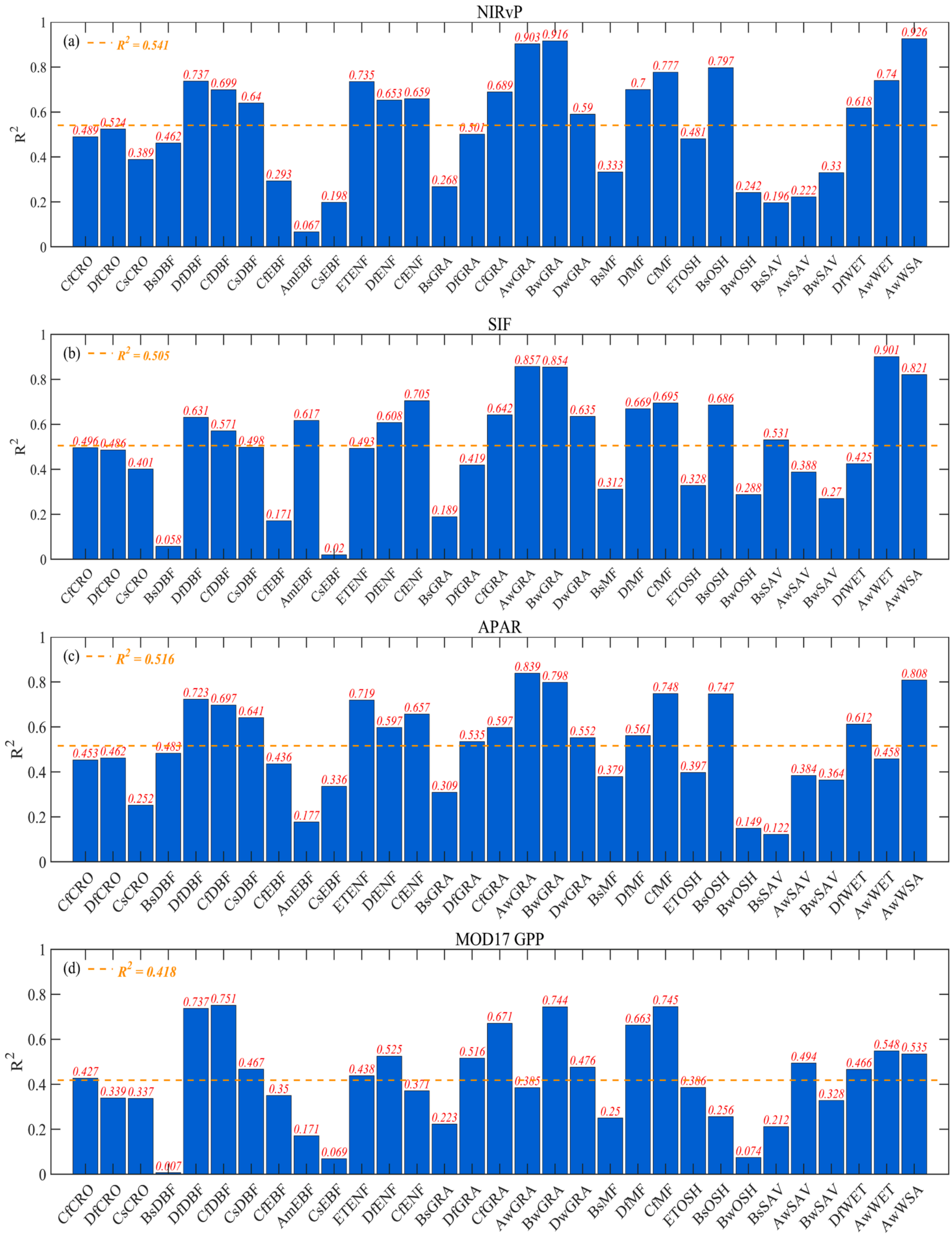

Fig. 5. Summary of the R^2 values of GPP proxies with EC GPP across the different biomes and climate zones in 147 FLUXNET sites (a, b, c, and d correspond to NIR_vP, SIF, APAR, and MOD17 GPP, respectively) (Horizontal dotted lines per panel denote the average R^2 value across all selected biomes and climate zones).

observed for the SAV and WSA biome after excluding the climate zone data.

3.3. Temporal variations in the environmental parameters, ρ_{NIR} and LUE

In order to obtain a better understanding of the existing correlations between ρ_{NIR} and LUE, the average multi-year environmental parameters, including PAR, air temperature (TA), and precipitation regime, and the corresponding values of EC GPP, NIR_vP, ρ_{NIR}, and LUE, were determined for analyzing the seasonal patterns. The correlation coefficients between ρ_{NIR} and LUE, and the environmental drivers at all the 147 selected sites were determined and enlisted in supplementary Table S5. Altogether, ρ_{NIR} was positively correlated with the LUE in 61.22% (90) of the sites, more than 50% (53) of these sites were significantly and positively correlated to the LUE (95% confidence level). The PAR, TA, and precipitation exhibited strong seasonal variations in the yearly

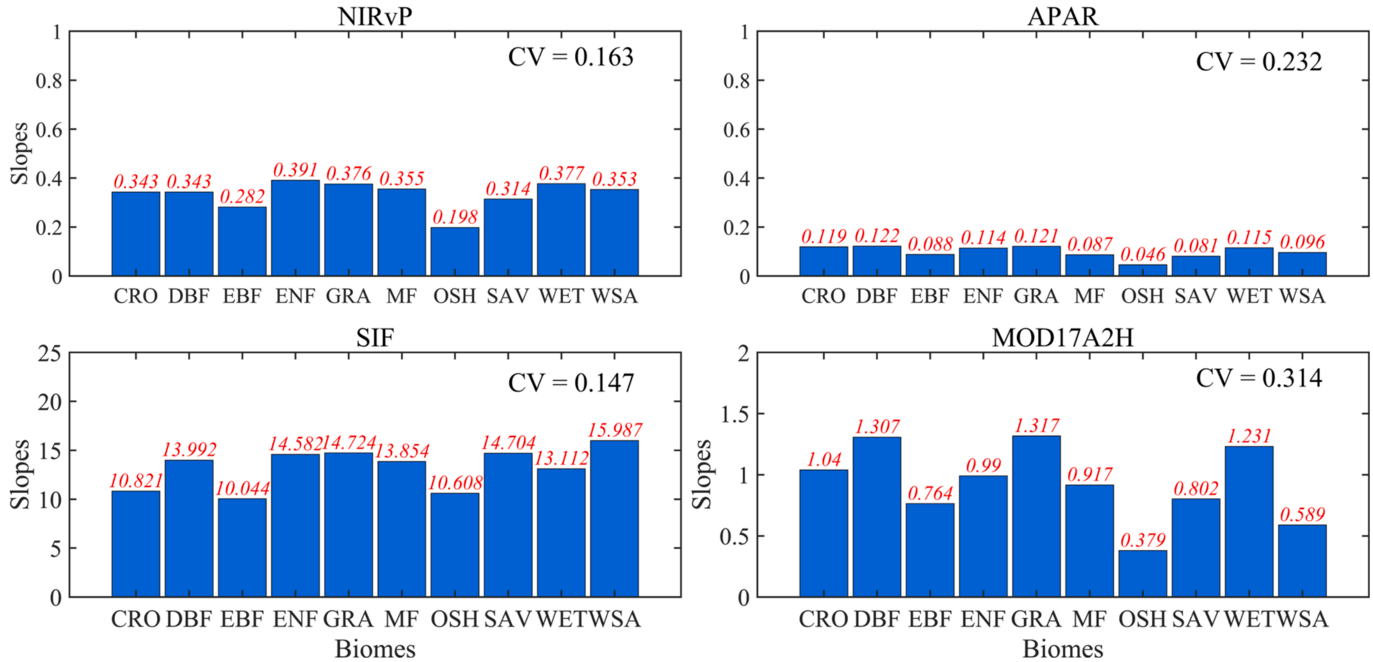

Fig. 6. Regression slopes and CV of NIR_vP, APAR, SIF, and MOD17A2H GPP with EC GPP across the different biomes.

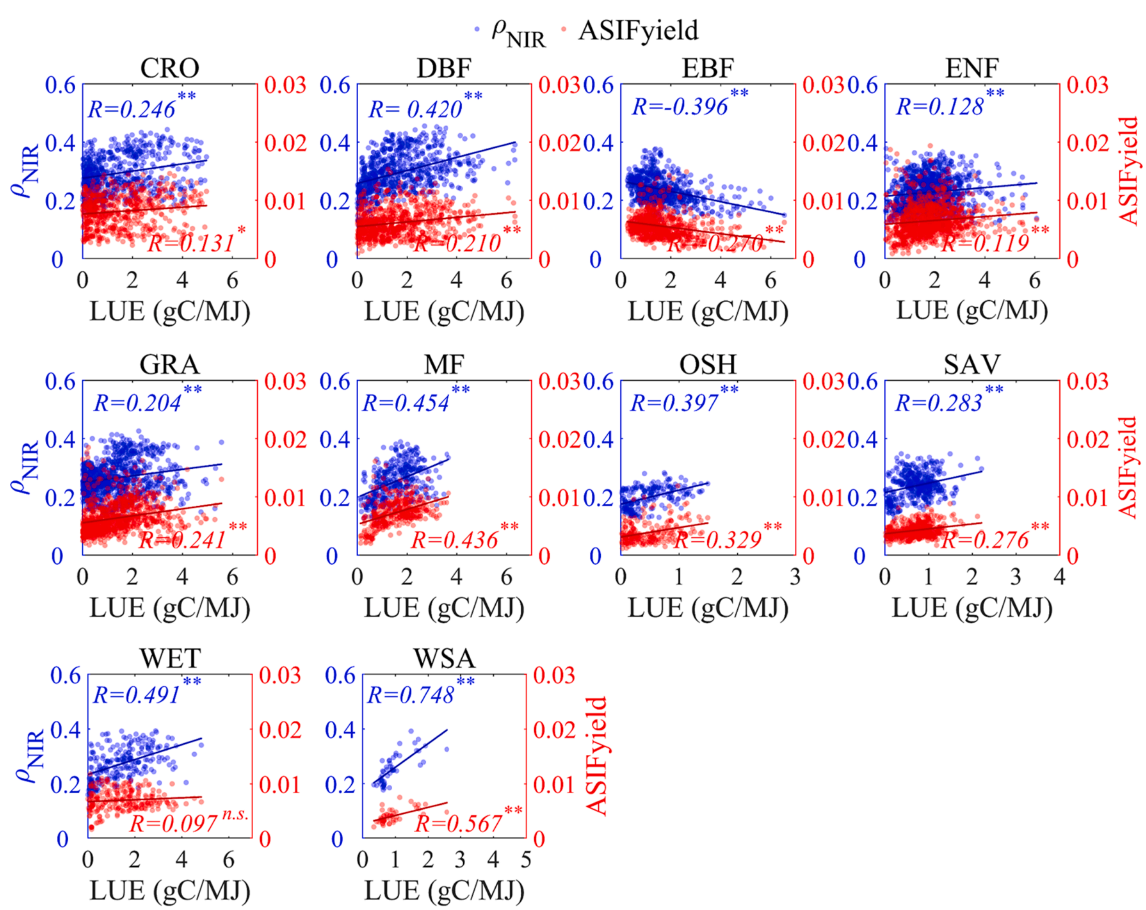

Fig. 7. Scatterplots depicting the values of ρ_{NIR} and $ASIF_{yield}$ versus LUE across different biomes at a 16-day scale over the FLUXNET sites. ρ_{NIR} and $ASIF_{yield}$ are depicted by red and blue scatter points, respectively. *p < 0.05 and **p < 0.001 indicate significant correlation; n.s. indicates no significant correlation (p > 0.05). (For interpretation of the references to color in this figure legend, the reader is referred to the web version of this article.)

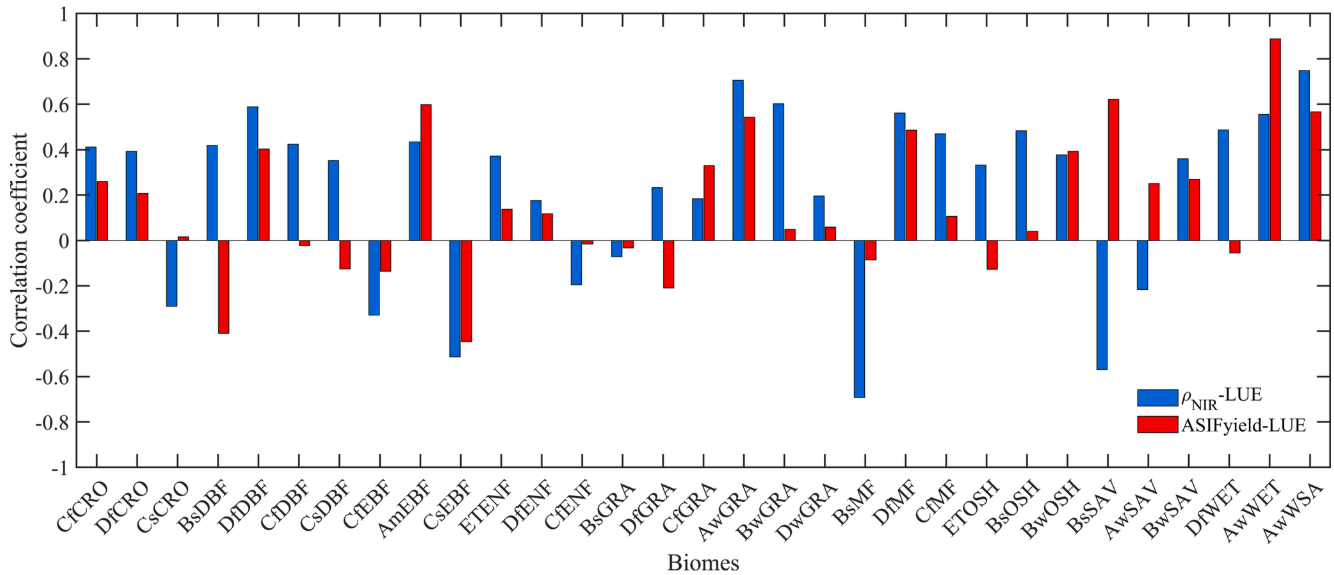

Fig. 8. The correlation coefficients of ρ_{NIR} and $ASIF_{yield}$ with LUE across different biomes and Köppen-Geiger climate zones.

meteorological patterns at these sites and exhibited covariations, which were also evident between the ρ_{NIR} and LUE. However, the ρ_{NIR} was negatively correlated to the LUE in 38.78% (57) of the 147 sites. The PAR, TA, and precipitation exhibited weak seasonal patterns in these sites and had variable differences with each other, and no seasonal covariance was observed between ρ_{NIR} and LUE.

Analysis of the relationship between TA and PAR revealed that the TA and PAR were positively correlated at all the sites, among which 146 (99.32%) sites were significantly and positively correlated (95% confidence level). The TA was positively correlated to the precipitation in 111 (75.50%) sites, but they were negatively correlated in 36 (24.49%) sites. Analysis of the PAR-precipitation relationship revealed that the parameters were positively correlated in 95 (64.63%) sites, but the PAR was negatively correlated to the precipitation in 52 (35.37%) sites.

4. Discussion

4.1. Influence of ρ_{NIR} on the NIR_vP-GPP relationship

In this study, we found that ρ_{NIR} could either positively or negatively drive the *NIR_vP*-GPP relationship, which varied with different biomes and climate zones. Numerous radiative transfer models (RTMs) have indicated that the variations in ρ_{NIR} were primarily associated with the LAI at the canopy level (Jacquemoud et al., 2000). Alterations in the PAR, TA, and precipitation also drive changes in vegetation phenology and LAI dynamics (Savoy et al., 2015; Smith et al., 2011). The findings indicated the existence of a covarying relationship between ρ_{NIR} and LUE if the vegetation growth curve agrees with favorable climate drivers. Altogether, we found ρ_{NIR} covaried with LUE at 90 (61.22 %) selected sites, having similar seasonal patterns of PAR, TA, and precipitation. Correspondingly, ρ_{NIR} was negatively correlated or even uncorrelated with LUE at 57 (38.78 %) selected sites, having different seasonal patterns of PAR, TA, and precipitation. These findings can partially explain the positive and the negative contribution attributed to ρ_{NIR} in the observed *NIR_vP* vs. GPP relationship.

Two typical sites where the ρ_{NIR} and LUE exhibited positive and negative correlations are illustrated for elucidating the seasonal patterns (Fig. S4). In a fully humid snowy climate of a DBF (DfDBF) site (site ID: US-Ha1), the PAR, TA, and precipitation, varied synchronously, so the ρ_{NIR} and LUE exhibited consistent variations throughout the year with a positive correlation coefficient of 0.785. On the contrary, the PAR, TA, and precipitation exhibited different seasonal patterns at an equatorial monsoon EBF (AmEBF) site (site ID: GF-Guy), and where ρ_{NIR} failed to track the variations in LUE giving a negative correlation coefficient of −0.414.

Therefore, although there was no discovery of a direct physical mechanism linking ρ_{NIR} with the LUE or GPP, we could still conclude that the robust *NIR_vP*-GPP relationship was co-attributed to both ρ_{NIR} and APAR, depending on the biome type and climatic conditions.

4.2. Differences among the performance of NIR_vP, SIF, APAR, and MOD17 GPP

In this study, we observed better *NIR_vP*-GPP relationships than SIF, APAR, and MOD17 GPP across most biomes and climate zones over the regions with similar seasonal patterns of PAR, TA, and precipitation. To further explore the importance of each proxy to GPP, we conducted multi-variable analysis based on GLM. Overall, we detected consistent phenomenon from GLM with the linear regression results, which also indicated a better *NIR_vP*-GPP relationship in most cases. However, it is worth noting that when putting three GPP proxies together, *NIR_vP* may not always be the most significant contributor to GPP.

In addition, we found the largest CV of linear regression slopes for MOD17 GPP with EC GPP, which was approximately 1/3 to 1/2 larger than *NIR_vP* and SIF (Fig. 6). The SIF-GPP relationship was similar but weaker than for *NIR_vP*, probably due to its relatively lower data quality, but it did display smallest CV because it represented physiological information. The *NIR_vP*-GPP relationship was shown to be more stable than APAR with lower CV. We conclude that this is mainly attributed to the contribution of ρ_{NIR} that reduces the variations of the *NIR_vP*-GPP relationship across different biomes. The worst performance of MOD17 GPP with EC GPP and the largest CV among other three proxies indicate that the MODIS approach to LUE-based modelling needs to be optimized or revised altogether.

4.3. Uncertainties

In this study, the mismatch between the satellite pixel size and local-scale flux footprint was corrected using a spatial scale correction ratio, but this discrepancy could not be fully eliminated. Therefore, this may induce uncertainties in the *NIR_vP*-GPP relationship, which partly explains the inconsistencies among the linear regression slopes across different biomes. In addition, the MCD15A2H FAPAR data could be a possible source of uncertainty due to the reported retrieval accuracy

(Tao et al., 2015), which could also introduce uncertainties during the quantification of the APAR and LUE.

Moreover, the basic equation for calculating NIR_vP was split into a combination of APAR, a ratio of NDVI/FAPAR, and ρ_{NIR} (Eq. (5)). Based on Eq. (5), we focused on the contribution of the additional information provided by ρ_{NIR} in NIR_vP, in addition to the role of APAR, while neglecting the variations in the NDVI/FAPAR ratio based on an assumed robust NDVI-FAPAR relationship (refer supplementary file, Fig. S2). However, the contribution of NDVI/FAPAR ratio on NIR_vP-GPP relationship was not investigated.

5. Conclusion

NIR_vP has been regarded as a promising proxy for GPP owing to the availability of records over long temporal periods and high data quality. However, the contribution of ρ_{NIR} contained in NIR_vP for estimating GPP across different biomes and climate zones has not been fully understood. Here, we investigated the NIR_vP-GPP relationship over different biomes and climate zones over 147 flux sites. We found that the correlation of NIR_vP with EC GPP was stronger than that of APAR, SIF, and MOD17A2H GPP across the majority of regions where the ρ_{NIR} was capable of tracking the variations in LUE. These regions usually have the same seasonal patterns for radiation, TA, and precipitation. In contrast, poorer performance of NIR_vP for tracking GPP was also found in certain regions where ρ_{NIR} failed to capture the LUE, and usually have different seasonal patterns of radiation, TA, and precipitation.

Overall, our study demonstrated the robustness of NIR_vP in GPP estimation and elucidated the limitations of NIR_vP in estimating GPP. We therefore recommend to consider whether ρ_{NIR} covariates with LUE when applying NIR_vP to GPP estimation over different regions.

Declaration of Competing Interest

The authors declare that they have no known competing financial interests or personal relationships that could have appeared to influence the work reported in this paper.

Data availability

No data was used for the research described in the article.

Acknowledgements

This work was supported by the National Key Research and Development Program of China (Grant No. 2022YFB3904801) and the National Natural Science Foundation of China (Grant No. 42071310).

Appendix A. Supplementary data

Supplementary data to this article can be found online at https://doi.org/10.1016/j.jag.2023.103437.

References

Abdi, A.M., et al., 2019. First assessment of the plant phenology index (PPI) for estimating gross primary productivity in African semi-arid ecosystems. Int. J. Appl. Earth Obs. Geoinf. 78, 249–260. https://doi.org/10.1016/j.jag.2019.01.018.

Agarwal, D.A., et al., 2010. A data-centered collaboration portal to support global carbon-flux analysis. Cconcurr. Comp.-Pract. E. 22 (17), 2323–2334. https://doi.org/10.1002/cpe.1600.

Badgley, G., et al., 2017. Canopy near-infrared reflectance and terrestrial photosynthesis. Sci. Adv. 3 (3), e1602244.

Badgley, G., et al., 2019. Terrestrial gross primary production: Using NIR_v to scale from site to globe. Glob. Chang. Biol. 25 (11), 3731–3740. https://doi.org/10.1111/gcb.14729.

Baldocchi, D., et al., 2001. FLUXNET: A new tool to study the temporal and spatial variability of ecosystem-scale carbon dioxide, water vapor, and energy flux densities. Bull. Am. Meteorol. Soc. 82 (11), 2415–2434. https://doi.org/10.1175/1520-0477(2001)082<2415:FANTTS>2.3.CO;2.

Baldocchi, D.D. et al., 2020. Outgoing near-infrared radiation from vegetation scales with canopy photosynthesis across a spectrum of function, structure, physiological capacity, and weather. J. Geophys. Res.: Biogeosci. 125(7), e2019JG005534. https://doi.org/10.1029/2019JG005534.

Ballantyne, A., á., et al., 2012. Increase in observed net carbon dioxide uptake by land and oceans during the past 50 years. Nature 488 (7409), 70–72. https://doi.org/10.1038/nature11299.

Cheng, R., et al., 2020. Decomposing reflectance spectra to track gross primary production in a subalpine evergreen forest. Biogeosciences 17 (18), 4523–4544. https://doi.org/10.5194/bg-17-4523-2020.

Coops, N.C., et al., 2010. Estimation of light-use efficiency of terrestrial ecosystems from space: A status report. Bioscience 60 (10), 788–797. https://doi.org/10.1525/bio.2010.60.10.5.

DAAC, O., 2018. MODIS and VIIRS Land Products Global Subsetting and Visualization Tool. ORNL DAAC, Oak Ridge, Tennessee, USA.

Dechant, B., et al., 2020. Canopy structure explains the relationship between photosynthesis and sun-induced chlorophyll fluorescence in crops. Remote Sens. Environ. 241, 111733 https://doi.org/10.1016/j.rse.2020.111733.

Dechant, B., et al., 2022. NIR_vP: A robust structural proxy for sun-induced chlorophyll fluorescence and photosynthesis across scales. Remote Sens. Environ. 268, 112763 https://doi.org/10.1016/j.rse.2021.112763.

Eyoh, A., et al., 2012. Modelling and predicting future urban expansion of Lagos, Nigeria from remote sensing data using logistic regression and GIS. Int. J. Appl. 2 (5), 58–71.

Frankenberg, C., et al., 2011. New global observations of the terrestrial carbon cycle from GOSAT: Patterns of plant fluorescence with gross primary productivity. Geophys. Res. Lett. 38 (17).

Garzón, J., et al., 2021. A Remote Sensing Approach for Surface Urban Heat Island Modeling in a Tropical Colombian City Using Regression Analysis and Machine Learning Algorithms. Remote Sens. 13 (21), 4256.

Geiger, R., 1961. berarbeitete Neuausgabe von Geiger, R: Köppen-Geiger/Klima der Erde. Wandkarte (wall map) 1 (16), 535. https://doi.org/10.1029/2011GL048738.

Gitelson, A.A., et al., 2016. Efficiency of chlorophyll in gross primary productivity: A proof of concept and application in crops. J. Plant Physiol. 201, 101–110. https://doi.org/10.1016/j.jplph.2016.05.019.

Gu, L., et al., 2019. Sun-induced Chl fluorescence and its importance for biophysical modeling of photosynthesis based on light reactions. New Phytol. 223 (3), 1179–1191. https://doi.org/10.1111/nph.15796.

Guanter, L., et al., 2014. Global and time-resolved monitoring of crop photosynthesis with chlorophyll fluorescence. Proc. Natl. Acad. Sci. 111 (14), E1327–E1333. https://doi.org/10.1073/pnas.1320008111.

Huete, A.R., 1988. A soil-adjusted vegetation index (SAVI). Remote Sens. Environ. 25 (3), 295–309. https://doi.org/10.1016/0034-4257(88)90106-X.

Jacquemoud, S., et al., 2000. Comparison of four radiative transfer models to simulate plant canopies reflectance: Direct and inverse mode. Remote Sens. Environ. 74, 471–481. https://doi.org/10.1016/S0034-4257(00)00139-5.

Jiang, C., et al., 2021. A daily, 250 m and real-time gross primary productivity product (2000–present) covering the contiguous United States. Earth Syst. Sci. Data 13 (2), 281–298. https://doi.org/10.5194/essd-13-281-2021.

Joiner, J., et al., 2013. Global monitoring of terrestrial chlorophyll fluorescence from moderate-spectral-resolution near-infrared satellite measurements: methodology, simulations, and application to GOME-2. Atmos. Meas. Tech. 6 (10), 2803–2823. https://doi.org/10.5194/amt-6-2803-2013.

Joiner, J., et al., 2016. New methods for the retrieval of chlorophyll red fluorescence from hyperspectral satellite instruments: simulations and application to GOME-2 and SCIAMACHY. Atmos. Meas. Tech. 9 (8), 3939–3967. https://doi.org/10.5194/amt-9-3939-2016.

Kim, J., et al., 2021. Solar-induced chlorophyll fluorescence is non-linearly related to canopy photosynthesis in a temperate evergreen needleleaf forest during the fall transition. Remote Sens. Environ. 258, 112362 https://doi.org/10.1016/j.rse.2021.112362.

Knyazikhin, Y., et al., 1998. Synergistic algorithm for estimating vegetation canopy leaf area index and fraction of absorbed photosynthetically active radiation from MODIS and MISR data. J. Geophys. Res. Atmos. 103 (D24), 32257–32275. https://doi.org/10.1029/98JD02462.

Köhler, P., et al., 2020. Global retrievals of solar-induced chlorophyll fluorescence at red wavelengths with TROPOMI. Geophys. Res. Lett. 47(15), e2020GL087541. https://doi.org/10.1029/2020GL087541.

Kottek, M., et al., 2006. World map of the Köppen-Geiger climate classification updated. Meteorol. Z. 15, 259–263. https://doi.org/10.1127/0941-2948/2006/0130.

Li, X., et al., 2019. Mapping photosynthesis solely from solar-induced chlorophyll fluorescence: A global, fine-resolution dataset of gross primary production derived from OCO-2. Remote Sens. 11 (21), 2563. https://doi.org/10.3390/rs11212563.

Lin, S., et al., 2021. Improved global estimations of gross primary productivity of natural vegetation types by incorporating plant functional type. Int. J. Appl. Earth Obs. Geoinf. 100, 102328 https://doi.org/10.1016/j.jag.2021.102328.

Lin, S., et al., 2022. Multi-site assessment of the potential of fine resolution red-edge vegetation indices for estimating gross primary production. Int. J. Appl. Earth Obs. Geoinf. 113, 102978 https://doi.org/10.1016/j.jag.2022.102978.

Liu, L., et al., 2019. Global white-sky and black-sky fapar retrieval using the energy balance residual method: Algorithm and validation. Remote Sens. 11 (9), 1004. https://doi.org/10.3390/rs11091004.

Liu, L., et al., 2020. Estimating maize GPP using near-infrared radiance of vegetation. Sci. Remote Sens. 2, 100009 https://doi.org/10.1016/j.srs.2020.100009.

Ma, Y., et al., 2022. An improved downscaled sun-induced chlorophyll fluorescence (DSIF) product of GOME-2 dataset. Eur. J. Remote Sens. 55 (1), 168–180. https://doi.org/10.1080/22797254.2022.2028579.

Major, D., et al., 1990. A ratio vegetation index adjusted for soil brightness. Int. J. Remote Sens. 11 (5), 727–740. https://doi.org/10.1080/01431169008955053.

McCree, K.J., 1972. Test of current definitions of photosynthetically active radiation against leaf photosynthesis data. Agric. Meteorol. 10, 443–453. https://doi.org/10.1016/0002-1571(72)90045-3.

Medlyn, B.E., 1998. Physiological basis of the light use efficiency model. Tree Physiol. 18 (3), 167–176. https://doi.org/10.1093/treephys/18.3.167.

Middleton, E.M., et al., 2016. 12 spectral bioindicators of photosynthetic efficiency and vegetation stress. Hyperspectral remote sensing of vegetation, CRC Press: 265-288. WOS:000355136500014.

Mitchell, J.J., et al., 2012. Remote sensing of sagebrush canopy nitrogen. Remote Sens. Environ. 124, 217–223. https://doi.org/10.1016/j.rse.2012.05.002.

Mohammed, G.H., et al., 2019. Remote sensing of solar-induced chlorophyll fluorescence (SIF) in vegetation: 50 years of progress. Remote Sens. Environ. 231, 111177 https://doi.org/10.1016/j.rse.2019.04.030.

Monteith, J., 1972. Solar radiation and productivity in tropical ecosystems. J. Appl. Ecol. 9 (3), 747–766. https://doi.org/10.2307/2401901.

Monteith, J.L., 1977. Climate and the efficiency of crop production in Britain. Philos. Trans. Royal Soc. London. Ser. B, Biol. Sci. 281 (980), 277–294. https://doi.org/10.1098/rstb.1977.0140.

Myneni, R., et al., 1994. On the relationship between FAPAR and NDVI. Remote Sens. Environ. 49 (3), 200–211. https://doi.org/10.1016/0034-4257(94)90016-7.

Myneni, R.B., et al., 2002. Global products of vegetation leaf area and fraction absorbed PAR from year one of MODIS data. Remote Sens. Environ. 83 (1–2), 214–231. https://doi.org/10.1016/0034-4257(94)90016-7.

Myneni, R., et al., 2005. MODIS/Terra+ Aqua Leaf Area Index/FPAR 8-day L4 Global 500m SIN Grid V006. NASA EOSDIS L. Process, DAAC.

Porcar-Castell, A., et al., 2014. Linking chlorophyll a fluorescence to photosynthesis for remote sensing applications: mechanisms and challenges. J. Exp. Bot. 65 (15), 4065–4095. https://doi.org/10.1093/jxb/eru191.

Running, S.W., et al., 2000. Global terrestrial gross and net primary productivity from the earth observing system. Methods in ecosystem science, Springer, New Yok 44–57. https://doi.org/10.1007/978-1-4612-1224-9_4.

Running, S. W. et al., 1999. MODIS daily photosynthesis (PSN) and annual net primary production (NPP) product (MOD17) Algorithm Theoretical Basis Document.

Running, S., et al., 2005. MOD17A2H MODIS/Terra Gross Primary Productivity 8-Day L4 Global 500m SIN Grid V006. https://doi. org/10.5067/MODIS.

Ryu, Y., et al., 2019. What is global photosynthesis? History, uncertainties and opportunities. Remote Sens. Environ. 223, 95–114. https://doi.org/10.1016/j.rse.2019.01.016.

Savoy, P., et al., 2015. Modeling the seasonal dynamics of leaf area index based on environmental constraints to canopy development. Agric. For. Meteorol. 200, 46–56. https://doi.org/10.1016/j.agrformet.2014.09.019.

Schaaf, C., et al., 2015. MCD43A4 MODIS/Terra+ Aqua BRDF/Albedo Nadir BRDF Adjusted RefDaily L3 Global 500 m V006. NASA EOSDIS Land Processes DAAC.

Smith, B., et al., 2011. A model of the coupled dynamics of climate, vegetation and terrestrial ecosystem biogeochemistry for regional applications. Tellus 63 (1), 87–106. https://doi.org/10.1111/j.1600-0870.2010.00477.x.

Sun, Y., et al., 2017. OCO-2 advances photosynthesis observation from space via solar-induced chlorophyll fluorescence. Science 358 (6360), eaam5747. https://doi.org/10.1126/science.aam5747.

Tao, X., et al., 2015. Assessment of five global satellite products of fraction of absorbed photosynthetically active radiation: Intercomparison and direct validation against ground-based data. Remote Sens. Environ. 163, 270–285. https://doi.org/10.1016/j.rse.2015.03.025.

van der Tol, C., et al., 2019. The scattering and re-absorption of red and near-infrared chlorophyll fluorescence in the models Fluspect and SCOPE. Remote Sens. Environ. 232, 111292 https://doi.org/10.1016/j.rse.2019.111292.

Vermote, E., et al., 1999. Atmospheric correction algorithm: spectral reflectances (MOD09). ATBD version 4, 1–107.

Wang, S., et al., 2020. Linking Photosynthetic Light Use Efficiency and Optical Vegetation Active Indicators: Implications for Gross Primary Production Estimation by Remote Sensing. ISPRS Ann. Photogramm., Remote Sens. & Spat. Infor. Sci. 5 (3), 571–578. https://doi.org/10.5194/isprs-annals-V-3-2020-571-2020.

Wang, S., et al., 2021. Tracking the seasonal and inter-annual variations of global gross primary production during last four decades using satellite near-infrared reflectance data. Sci. Total Environ. 755, 142569 https://doi.org/10.1016/j.scitotenv.2020.142569.

Wilks, D.S., 2011. Statistical methods in the atmospheric sciences, Vol. 100. Academic Press.

Wohlfahrt, G., et al., 2018. Sun-induced fluorescence and gross primary productivity during a heat wave. Sci. Rep. 8 (1), 1–9. https://doi.org/10.1038/s41598-018-32602-z.

Xiao, J., et al., 2019. Remote sensing of the terrestrial carbon cycle: A review of advances over 50 years. Remote Sens. Environ. 233, 111383 https://doi.org/10.1016/j.rse.2019.111383.

Yang, P., et al., 2019. Using reflectance to explain vegetation biochemical and structural effects on sun-induced chlorophyll fluorescence. Remote Sens. Environ. 231, 110996 https://doi.org/10.1016/j.rse.2018.11.039.

Yang, P., et al., 2022. Evolution of light use efficiency models: Improvement, uncertainties, and implications. Agric. For. Meteorol. 317, 108905 https://doi.org/10.1016/j.agrformet.2022.108905.

Yuan, W., et al., 2014. Global comparison of light use efficiency models for simulating terrestrial vegetation gross primary production based on the LaThuile database. Agri. Forest Meteorol. 192, 108–120. https://doi.org/10.1016/j.agrformet.2014.03.007.

Zeng, Y., et al., 2019. A practical approach for estimating the escape ratio of near-infrared solar-induced chlorophyll fluorescence. Remote Sens. Environ. 232, 111209 https://doi.org/10.1016/j.rse.2019.05.028.

Zhang, Z., et al., 2020. The potential of satellite FPAR product for GPP estimation: An indirect evaluation using solar-induced chlorophyll fluorescence. Remote Sens. Environ. 240, 111686 https://doi.org/10.1016/j.rse.2020.111686.

Zhang, Z., et al., 2021. Sensitivity of estimated total canopy SIF emission to remotely sensed LAI and BRDF products. J. Remote Sens. 2021. https://doi.org/10.34133/2021/9795837.